

Towards Image Semantics and Syntax Sequence Learning

Chun Tao

School of Electrical and Computer Engineering
Purdue University
465 Northwestern Ave, West Lafayette, IN 47907
tao88@purdue.edu

Timur Ibrayev

School of Electrical and Computer Engineering
Purdue University
West Lafayette, IN 47907
tibrayev@purdue.edu

Kaushik Roy

School of Electrical and Computer Engineering
Purdue University
465 Northwestern Ave, West Lafayette, IN 47907
kaushik@purdue.edu

Abstract

Convolutional neural networks and vision transformers have achieved outstanding performance in machine perception, particularly for image classification. Although these image classifiers excel at predicting image-level class labels, they may not discriminate missing or shifted parts within an object. As a result, they may fail to detect corrupted images that involve missing or disarranged semantic information in the object composition. On the contrary, human perception easily distinguishes such corruptions. To mitigate this gap, we introduce the concept of "image grammar", consisting of "image semantics" and "image syntax", to denote the semantics of parts or patches of an image and the order in which these parts are arranged to create a meaningful object. To learn the image grammar relative to a class of visual objects/scenes, we propose a weakly supervised two-stage approach. In the first stage, we use a deep clustering framework that relies on iterative clustering and feature refinement to produce part-semantic segmentation. In the second stage, we incorporate a recurrent bi-LSTM module to process a sequence of semantic segmentation patches to capture the image syntax. Our framework is trained to reason over patch semantics and detect faulty syntax. We benchmark the performance of several grammar learning models in detecting patch corruptions. Finally, we

verify the capabilities of our framework in Celeb and SUN-RGBD datasets and demonstrate that it can achieve a grammar validation accuracy of 70 to 90% in a wide variety of semantic and syntactical corruption scenarios.

1. Introduction



Figure 1. ViT-B/16,224 tested on corrupted dog images. Corruptions from left to right: 1) permutation type I 2) permutation type II 3) 1-patch blackout 4) 2-patch Gaussian blurring, kernel size= (7, 7), sigma= 3. All top-5 predictions are dog breeds, shown as softmax-ed probabilities

Current image classification techniques involve training Deep Neural Networks (DNN) to extract high-dimensional

features from the entire image and then decode the features to produce class predictions. For such classification tasks, Convolutional Neural Networks (CNNs) [22, 31, 45] and Vision Transformers (ViTs) [13, 38] are state-of-the-art (SoTA) models. CNNs learn the distribution of images belonging to different object classes by extracting low- and high-level semantic information from images and encoding them in hidden features of different layers [24, 40]. They can also be trained to effectively detect out-of-distribution (OOD) anomalies [8, 55]. Different from OOD anomalies, samples with syntactical anomalies (corruptions) do not introduce new semantics, but are noisy in-distribution (ID) samples [40, 54]. CNNs have been shown to consistently produce high confidence in the classification of these samples [1, 63]. Although research have shown that ViTs tend to make better predictions on these samples than CNNs [14, 47, 65], they may still not be able to identify in-distribution corruptions. Fig.1 shows the test results of a vit-base-patch16-224 model pretrained on ImageNet [11] on 2 random dog images from the Stanford Dogs dataset [29]. For the semantically and (or) syntactically corrupted images (in-distribution samples), the top 5 most probable classes predicted by the ViT model are always dog breeds, out of 1000 classes in ImageNet. We further verified this result on all 8580 test set images. The results indicate that current image classifiers are vulnerable to object-level semantic and syntactical in-distribution corruptions. In this work, we tackle noisy in-distribution samples that involve object- and scene-centric [44] semantic corruptions such as patch shuffling, blackout, blurring, etc.

To address the above issues, a "grammar" analysis of the image is necessary. The concept of **image grammar** consists of **image semantics and image syntax**, analogous to their counterparts in the language domain [17, 50]. While "image semantics" refers to individual meaning and significance of parts that compose a valid object [43], "image syntax" defines the spatial positioning and arrangement of these part semantics that reside in an object to align with the well-formed object composition of a given class [5]. An effective machine learning (ML) system capable of recognizing part-level image corruptions will then need to be trained to **1)** extract pixel-wise semantics from the content of the input image and **2)** sequentially visit the learned semantics patch by patch to verify whether the relative positioning of these patches is correct with respect to the object class of interest. We illustrate syntax learning with part semantic information in Fig.2. In glimpse 1 of Fig.2, we show a patch of the human face on the left and its semantic components belonging to the "face", "nose", and "mouth" classes on the right. The semantic segmentation of the patch is called part semantics. When the model shifts up from the current patch to glimpse 2, new part semantics belonging to the "eyes", "eyebrow", and "hair" classes appear. The transition from

the part semantics of glimpse 1 to that of glimpse 2 represents an episode of the syntax sequence of the "human face" object class.

We propose a weakly-supervised two-stage *deep learning framework* that successively learns part semantics and image syntax as described above. In the **first** stage, we utilize a feature extractor network (Feature Pyramid Network (FPN) with CNN backbone) to produce pixel-wise semantic features. The FPN is fine-tuned on a small number of semantic segmentation masks, generated using deep clustering technique [6], a visual representation learning tool. The idea is to iteratively 1) cluster pixel-wise features 2) minimize distance between these features and the centroid vectors they are assigned to. The latter step ensures that the feature extractor network learns to produce features that align better with the existing bank of centroids, each representing a semantic concept, in the next iteration. Pixel-level features become cluster-friendly throughout training iterations and are mapped to their corresponding semantics. We further adopt augmentation to enhance color invariance and geometric equivariance in clustering results [9]. The first stage helps divide the object in an image into segmentations of semantically rich parts. In the **second** stage, we first fine-tune the feature extractor on the semantic masks of the parts. Then, we define a patch traversal sequence for all images containing the same object. Patch traversal iterates through image part patches in a fixed order in order to construct a sequence of part semantic masks. For each image, we feed the sequence of part semantic masks to a recurrent bi-LSTM module, following the traversal rules we have defined (Fig.3). In a bi-LSTM, we utilize the long-short-term memory to handle bi-directional dependencies in the sequence of image part semantics and, consequently, to learn image syntax. Finally, during the test phase, agnostic to the corrupt state of the input image, the bi-LSTM module traverses the part semantics of patches in the same order defined earlier and aggregates its prediction error. For each image, the total prediction error is thresholded to detect potential corruptions. Note that we do not train our pipeline on any of the noisy in-distribution samples described above but only on samples with correct grammar. However, the pipeline utilizes its knowledge of the semantics of the parts of the image and the syntax of the image to check the grammar correctness of the test images.

Our key contributions include:

1. Image grammar analyses to verify class label integrity of noisy in-distribution samples;
2. A weakly-supervised two-stage learning system that combines pixel-wise semantic extraction and syntax sequence learning to capture image grammar with respect to an object/scene class; Testing the capability of the system in detecting in-distribution anomaly samples;
3. Benchmarking the effectiveness of several image gram-

mar validation methods on two datasets.

2. Related Work

Performing image grammar analysis for visual objects requires a combination of visual semantic perception and understanding and reasoning in the context. Below, we investigate perspectives around the capabilities of CNNs and ViTs in handling the above functionalities.

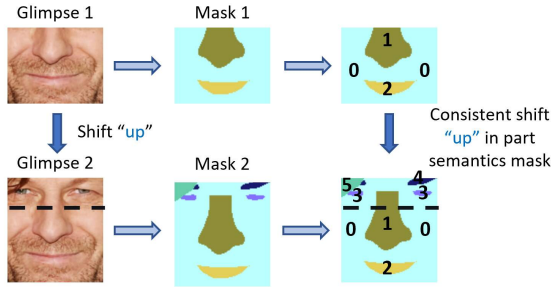


Figure 2. Illustration of a transition in patch sequence and its consistent shift in semantic segmentation

Self-Supervised Visual Representation Learning and Feature Clustering To extract semantics from an image, visual representation learning is required, in which meaningful and compact features are extracted from raw visual data. A number of early works have combined layers of weights to produce deep supervised predictors, including neural networks [3, 4]. Since then, convolutional neural networks (CNNs) [22, 31, 45] have been extensively applied for the extraction of vision features. CNNs are capable of learning hierarchical features. As a result of their ability to capture both low-level and high-level features, they enable better generalization. More recently, ViTs encode representation of fine and coarse structures in patch embeddings. [12]. They effectively capture long-range dependencies across patches through the self-attention mechanism [34, 38]. In view of the arduous nature of data labeling, researchers have developed methods of unsupervised and self-supervised learning (SSL) [23, 51, 53, 58, 61]. To enhance semantic learning with CNN, ViT, and Autoencoder(AE) models, these contrastive learning methods ensure full use of correlations between features across views or patches. Additionally, contrastive learning is often coupled with clustering and pseudo-labeling in SSL approaches [6, 7, 15]. Authors in [18, 56, 59] first integrated image clustering and representation learning into a single model. *DeepCluster* [6] iteratively groups features with K-means clustering algorithm and uses the subsequent assignments as a supervision for updating the feature extractor network. Deep clustering makes feature representation learning suitable for clustering tasks [18, 52, 62].

Weakly-supervised Part Semantic Segmentation Joint clustering and feature learning methods are naturally suitable for unsupervised semantic segmentation tasks, especially for datasets that are *semantically homogeneous*. The segmentation result depends on the scale and granularity of the homogeneous semantic concepts within the dataset. When the dataset is **object-centric** such as CelebA with aligned faces, the semantic segmentation task reduces to clustering pixel-level features, resulting in object-part (face parts) segmentation; whereas when the dataset is **scene-centric**, like SUN-RGBD with different room layouts, adopting the same pixel-level semantic segmentation results in common stuff (floor, wall, ceiling, etc.) and things (desk, table, chair, etc.) segmentation. A few unsupervised semantic segmentation approaches involving clustering have emerged in past years. The authors in [2, 26, 42] iteratively refine their model weight with deep clustering, spatial consistency, and contrastive learning. For our semantics-learning purpose, we chose to implement a modified version of PiCIE [9], thanks to the adjustable granularity of its pixel segmentation and universality to segment both "stuff" and "things". Similar to distilled feature correspondence in [20] and mask proposals in [49], in our experiments on CelebA we add a visual prior to our pixel-level features by finetuning the feature extractor model on coarse CelebAHQ [32] masks, before deep clustering training. This leads to human-recognizable semantic masks of face parts as shown in Fig.3.

Image Grammar Validation with Sequential Models

There is evidence that CNNs and ViTs do not tend to alter their classifications when images are naturally corrupted [16, 19, 48, 64]. While CNNs may not distinguish positional disruptions among patches due to its translational invariance [48, 64], this trend is more pronounced for ViTs, as the attention mechanism ignores patch corruptions while focusing on the main foreground for prediction [16, 19]. As shown in Fig.1, we verified this behavior of ViTs. This means that these image classifiers are unable to reason over patch semantics, construct proper grammar, and detect in-distribution grammar corruptions. The use of recurrent neural networks (RNNs) appears an ideal solution to this problem. Previously, RNNs have been used to process image patches sequentially. The RAM [39] takes into account fixations around different locations within the image one at a time, and combines the information into a more dynamic scene representation. Other works used LSTM models to selectively attend to parts of the image while performing retrieval tasks [36, 57]. Our work involves encoding sequential image syntax learning in a bi-LSTM model based on an individual object or scene class. During training, it learns to predict patch semantics based on neighboring semantics in the syntactical sequence, and during testing, it detects in-distribution anomalies based on its predictions.

3. Method

In this section, we describe the training and test methods adopted in our grammar validation pipelines, illustrated in Fig.3, 4. To begin with, we assume that the objects inside input images are localized with techniques such as [10, 25]. Such an assumption matches the requirement that the dataset needs to be semantically homogeneous: it only contains images that consist of a single uniform class (either a class of objects or scenes). Aligned CelebA and SUN-RGBD both meet this criterion. Once localized images are obtained, we propose 2 stages of processing: **1)** part semantic clustering and **2)** image syntax learning. The realization of each stage is discussed below.

3.1. Stage 1: Part Semantic Clustering

To fully understand the semantics of parts inside an image containing a localized object, the unlabeled input images are mapped to their semantic segmentation at the pixel level. To automate semantic learning and train these visual features with little supervision, deep clustering [6, 9] is used: alternately cluster the most recent features and then use cluster assignments as pseudo-labels to refine the feature extractor model. Despite the appeal of an unsupervised setting, semantic richness on the part level cannot be guaranteed. In our empirical study, deep clustering results in segmentation that only separates the entire object from the background (e.g., in CelebA, the entire face is rendered as a single cluster). This is due to greater variation in color between the object and the background than among parts within the object itself. In order to extract part semantics from the DNN feature extractor, we fine-tune it under weak supervision from a subset of pixel-level segmentation masks. We map ground truth (GT) masks to coarse classes to represent part semantics.

Suppose that we have input images $x_i, i = 1, \dots, N$ and a subset of them has pixel-level annotations $m_{jp}, j = 1, \dots, M, M \ll N$. Let us assume that we have C semantic classes in the preprocessed ground-truth (GT) annotations and $\forall j, p, m_{jp} \in [0, 1, \dots, C - 1]$. The feature extractor has an embedding function f_θ , which produces pixel-level feature vectors $z_{ip} = f_\theta(x_i)[p], z_{ip} \in \mathbb{R}^d$.

During the fine-tuning phase, we feed pixel-level embedding features to a parametric linear classifier $g_\omega, \omega \in \mathbb{R}^{d \times C}$, so that the feature dimensions are projected onto the number of semantic classes C . For all images x_j that have GT masks, the resulting pixel-level prediction becomes $g_\omega(z_{jp})$. To fine-tune the feature extractor to have a part semantics visual prior, we minimize the cross entropy loss between pixel-level prediction $g_\omega(z_{jp})$ and GT segmenta-

tion mask m_{jp} , we optimize the following:

$$\min_{\theta, \omega} \mathcal{L}_{CE}(g_\omega(f_\theta(x_j)[p]), m_{jp}) \quad \text{where}$$

$$\mathcal{L}_{CE} = -\log \frac{\exp(g_\omega(z_{jp})[m_{jp}])}{\sum_{k=0}^{C-1} \exp(g_\omega(z_{jp})[k])} \quad (1)$$

We can discard the classifier once the feature extractor has been fine-tuned and improved by part semantics prior. Now, we begin DeepCluster training with practices outlined in [9] so that the model can automatically distinguish the most reasonable part semantics.

To get a semantic grouping of pixels, in PiCIE training [9] inductive biases are added in the form of photometric invariance and geometric equivariance. Photometric transformations include color jittering and are denoted P , while geometric transformations refer to random cropping and flipping, denoted G . As demonstrated in Fig.3, trained images are sampled into 2 transformation streams. First, for an input image x_i , photometric transformations $P_i^{(1)}$ and $P_i^{(2)}$ are applied in each of the streams. An additional geometric transform $G_i^{(2)}$ is applied in the bottom stream. Afterward, both $P_i^{(1)}(x_i)$ and $G_i^{(2)}(P_i^{(2)}(x_i))$ are fed to the fine-tuned feature extractor before the scaled geometric transformation $G_i^{(1)}$ is applied to feature map in the top stream in Fig.3.

Because the feature map is reduced in width and height compared to the original image, the cropping transform in $G_i^{(2)}$ is scaled with the same ratio to obtain $G_i^{(1)}$. We then have pixel-level features ready to cluster in top and bottom streams denoted as,

$$z_{ip}^{(1)} = G_i^{(1)}(f_\theta(P_i^{(1)}(x_i)))[p] \quad (2)$$

$$z_{ip}^{(2)} = f_\theta(G_i^{(2)}(P_i^{(2)}(x_i)))[p] \quad (3)$$

The pixel-level features in each stream are clustered with K-means algorithm. We apply overclustering and determine the number of clusters K . The K-means clustering loss becomes,

$$\mathcal{L}_{Kmeans} = \sum_{i=1}^N \sum_p \sum_{k=1}^K \|z_{ipk} - \mu_k\|^2 \quad (4)$$

where μ_k is the k -th centroid. By optimizing the loss in 4 until it converges, we have cluster assignments \mathbf{y}' and a centroid matrix $\boldsymbol{\mu}$ for each stream,

$$\mathbf{y}'^{(1)}, \boldsymbol{\mu}^{(1)} = \arg \min_{\mathbf{y}', \boldsymbol{\mu}} \sum_{i=1}^N \sum_p \|z_{ip}^{(1)} - \mu_{y'_{ip}}^{(1)}\|^2 \quad (5)$$

$$\mathbf{y}'^{(2)}, \boldsymbol{\mu}^{(2)} = \arg \min_{\mathbf{y}', \boldsymbol{\mu}} \sum_{i=1}^N \sum_p \|z_{ip}^{(2)} - \mu_{y'_{ip}}^{(2)}\|^2 \quad (6)$$

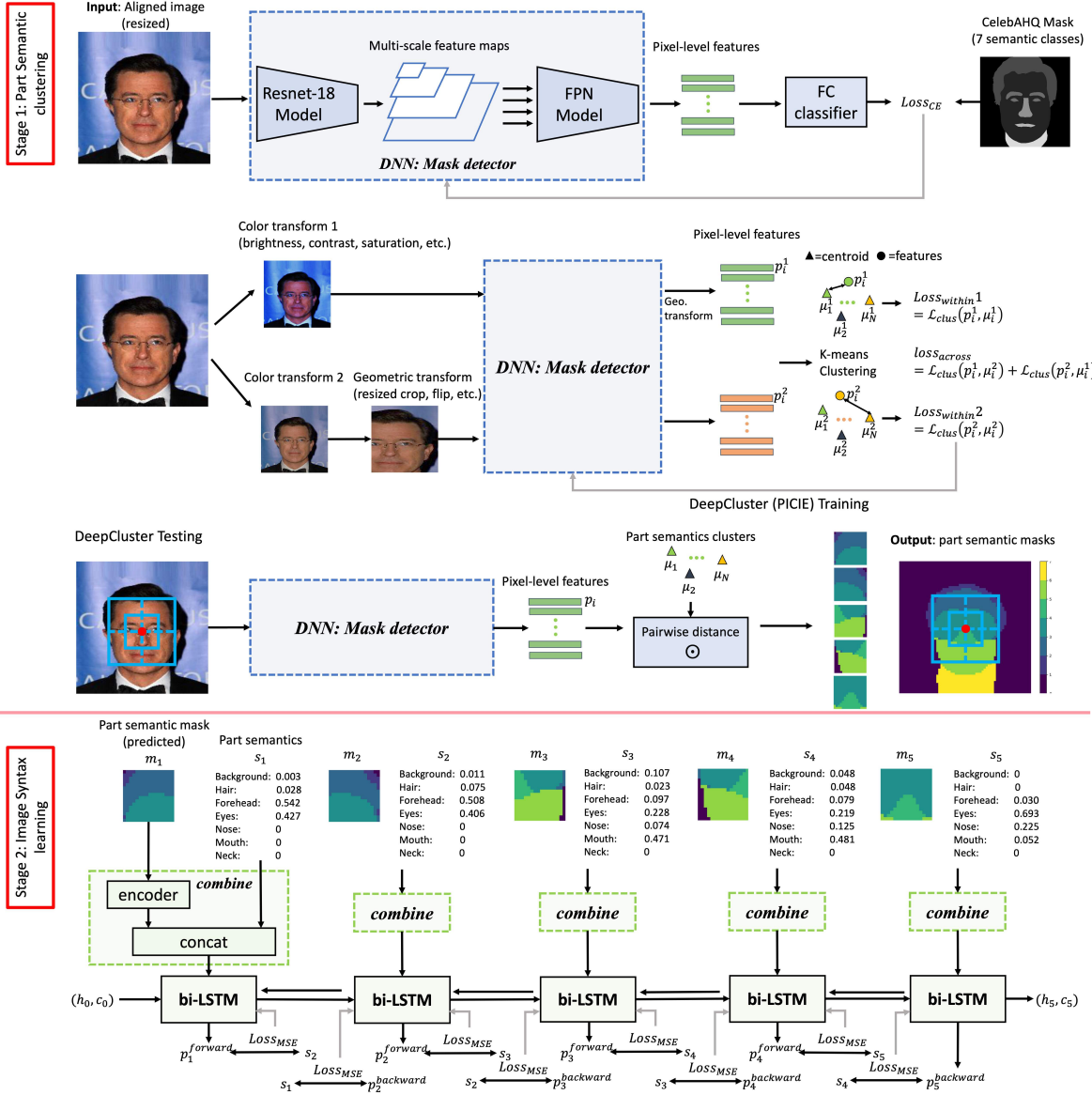


Figure 3. Training pipeline

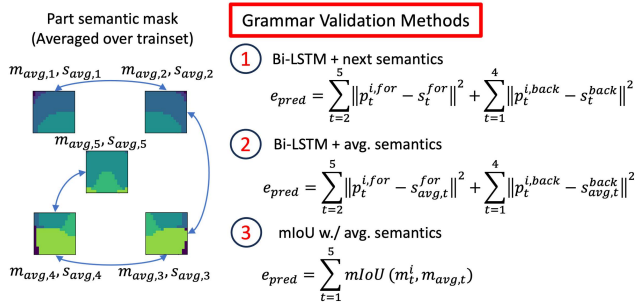


Figure 4. Test methods for grammar validation

We follow the same mechanism for computing cluster losses as specified in PiCIE [9]. To avoid insufficiently trained classifiers and their noisy gradients, we abandon the

parametric classifier g_ω and instead compute the distance between the pixel-level features z_{ip} and the centroids μ as a DeepCluster loss. We train the feature extractor model with the following DeepCluster (DC) objective,

$$\min_{\theta} \sum_{i=1}^N \sum_p \mathcal{L}_{DC}(z_{ip}, y'_{ip}, \mu) \quad \text{where}$$

$$\mathcal{L}_{DC}(z_{ip}, m_{ip}, \mu) = -\log \frac{\exp(-d(z_{ip}, \mu_{y'_{ip}}))}{\sum_{k=1}^K \exp(-d(z_{ip}, \mu_k))} \quad (7)$$

$d(\cdot, \cdot)$ is the cosine distance. The total PiCIE [9] loss is composed of 2 parts. 1) in each of the top and bottom streams, the feature vectors are expected to adhere to their cluster-

ing labels, so that they can encode the same semantic concepts in each of the banks of clusters. That loss is called the "within" loss. 2) to ensure that the clustering result is invariant to P and equivariant to G , feature vectors from one stream are expected to match cluster assignments and centroids of the other; thus a "cross" loss is incurred. The total loss $\mathcal{L}_{total} = \mathcal{L}_{within} + \mathcal{L}_{cross}$, where

$$\mathcal{L}_{within} = \sum_{i=1}^N \sum_p \mathcal{L}_{DC}(z_{ip}^{(1)}, y'_{ip}^{(1)}, \boldsymbol{\mu}^{(1)}) \quad (8)$$

$$+ \mathcal{L}_{DC}(z_{ip}^{(2)}, y'_{ip}^{(2)}, \boldsymbol{\mu}^{(2)})$$

$$\mathcal{L}_{cross} = \sum_{i=1}^N \sum_p \mathcal{L}_{DC}(z_{ip}^{(1)}, y'_{ip}^{(2)}, \boldsymbol{\mu}^{(2)}) \quad (9)$$

$$+ \mathcal{L}_{DC}(z_{ip}^{(2)}, y'_{ip}^{(1)}, \boldsymbol{\mu}^{(1)})$$

3.2. Stage 2: Image Syntax Learning

In this stage, we learn image syntax, which is the arrangement of parts that create a meaningful image. Analogous to syntax in the language domain, we expect certain semantic patterns to display sequentiality within an image. Depending on how the image is traversed and the size of the image patches, the semantics sequence may be too diverse to be learned in an image syntax study. Hence, it is necessary to determine the traversal rules for a particular class of objects before learning the image syntax.

Shown in Fig.5 and 8 are the traversal rules we decided for faces and for room layouts. Because faces are localized in aligned CelebA (object-centric), we apply five crops around the center point of the image, and circularly transit among these patches. For room layouts in the SUN-RGBD dataset (scene-centric), we zig-zag through the image patches from top to bottom, left to right.

Having established the traversal scheme, we begin constructing the image syntax. Note that the syntax-learning system learns sequences of part semantics from natural images and generalizes that knowledge to detect anomalies in wild images. **In training, we do not include any corrupted images.** For image $x^{(i)}$, $i = 1, \dots, N$ and patch id t , $t = 1, \dots, G$, where G refers to the number of patches, we resize and crop an image patch $x_t^{(i)}$ and its corresponding semantic segmentation at the pixel level $m_t^{(i)}$. The p^{th} pixel has the semantic class $m_{tp}^{(i)}$. For each $m_{tp}^{(i)}$, we prepare its semantic vector $s_t^{(i)}$ by computing the proportion of each semantic class in its flattened form.

To process image part semantics sequentially and learn image syntax, we employ a recurrent neural network (RNN). Specifically, as both directions in the traversal of part semantics are valid sequences to be learned, we use a bi-directional Long Short-Term Memory (bi-LSTM), parameterized by $\mathbf{W} = \{W_i, W_f, W_g, W_o\}$ and $\mathbf{b} =$

$\{b_i, b_f, b_g, b_o\}$. For an input image x_i , we traverse each of its crop masks $m_t^{(i)}$, $t = 1, \dots, G$. The input $\hat{x}_t^{(i)}$ in timestep t is the concatenation of the encoded part semantic mask $m_t^{(i)}$ (positional and semantic cues) and a semantics vector $s_t^{(i)}$ (semantic cue). At timestep t , the bi-LSTM model has 2 predictions, $p_t^{(i,for)} = L_{\mathbf{W},\mathbf{b}}(\hat{x}_t^{(i)}, h_t^{(i,for)})$ for the next semantics $s_{t+1}^{(i)}$ and $p_t^{(i,back)} = L_{\mathbf{W},\mathbf{b}}(\hat{x}_t^{(i)}, h_t^{(i,back)})$ for the previous semantics $s_{t-1}^{(i)}$. Across the set of train images \mathbf{x} , the learning goal of bi-LSTM is to capture the transition patterns between image part semantics by increasing the probability of the set of semantic vectors \mathbf{s}_t to appear in the timestep t , based on neighboring patch inputs $\hat{\mathbf{x}}_{t-1}$ and $\hat{\mathbf{x}}_{t+1}$, and neighboring hidden states h_{t-1}^{for} and h_{t+1}^{back} that include information in all inputs \hat{x}_j , $\forall j \neq t$. Throughout the dataset, we try to model the conditional probability assuming a Gaussian distribution on the set of semantic vectors \mathbf{s}_t in the timestep t .

$$\begin{aligned} \mathbb{P}(\mathbf{s}_t | \hat{\mathbf{x}}_{t-1}, \hat{\mathbf{x}}_{t+1}, \mathbf{h}_{t-1}^{for}, \mathbf{h}_{t+1}^{back}) \quad (10) \\ = \mathbb{P}(\mathbf{s}_t | \hat{\mathbf{x}}_j, \forall j \neq t) \\ = \mathcal{N}(\mathbf{s}_t; \mathbf{p}_t(\hat{\mathbf{x}}_j, \forall j \neq t; \mathbf{W}, \mathbf{b}), \sigma_t^2) \end{aligned}$$

In Eq.10 \mathbf{p}_t is the model's prediction of the vector mean of the distribution of \mathbf{s}_t . The Gaussian distribution in Eq.10 has a probability density function (PDF) $p(s_t^{(i)}; p_t^{(i)}, \sigma_t^2) = \frac{1}{\sqrt{2\pi\sigma_t^2}} \exp(-\frac{1}{2} \frac{(s_t^{(i)} - p_t^{(i)})^2}{\sigma_t^2})$. We transform the conditional probability in Eq.10 to log-likelihood by replacing it with the aforementioned Gaussian PDF and using properties of the logarithm,

$$\begin{aligned} \sum_{i=1}^N \log \mathbb{P}(s_t^{(i)} | \hat{x}_j^{(i)}, \forall j \neq t; \mathbf{W}, \mathbf{b}) \quad (11) \\ = -N \log \sigma_t - \frac{N}{2} \log(2\pi) - \sum_{i=1}^N \frac{\|p_t^{(i)} - s_t^{(i)}\|^2}{2\sigma_t^2} \end{aligned}$$

If we adopt maximum log-likelihood estimation (MLE) on Eq.11, it's equivalent to minimizing the MSE loss between the model's prediction at timestep t , p_t , and the actual semantics s_t . We thus have the following optimization objective for the bi-LSTM model,

$$\begin{aligned} \min_{\mathbf{W}, \mathbf{b}} \sum_{i=1}^N \sum_{t=1}^G \|p_t^{(i)} - s_t^{(i)}\|^2 \quad (12) \\ = \min_{\mathbf{W}, \mathbf{b}} \sum_{i=1}^N \left(\sum_{t=2}^G \|p_t^{(i,for)} - s_t^{(i)}\|^2 + \sum_{t=1}^{G-1} \|p_t^{(i,back)} - s_t^{(i)}\|^2 \right) \end{aligned}$$

where $p_t^{(i,for)}$ and $p_t^{(i,back)}$ are the bi-LSTM predictions in forward and backward-direction streams.

During test, both correct and corrupted images are used as input. For any input image patch, pixel-wise semantic segmentation must be produced faithfully. In Fig.3,

we include fine-tuning of the feature extractor f_θ and classifier g_ω on resized image patch crops $x_{ig}, i = 1, \dots, N, t = 1, \dots, G$. We use resized patch masks cropped from the output of stage 1, m_{itp} , as supervision. Thus, we have the following pixel-level cross-entropy loss minimization:

$$\min_{\theta, \omega} \mathcal{L}_{CE}(g_\omega(f_\theta(x_{it})[p]), \hat{y}_{itp}) \quad \text{where} \quad (13)$$

$$\mathcal{L}_{CE} = -\log \frac{\exp(g_\omega(z_{itp})[\hat{y}_{itp}])}{\sum_{k=0}^{C-1} \exp(g_\omega(z_{itp})[k])}$$

We present 3 test methods for grammar validation in Fig.4. We first prepare averaged part semantic masks and vectors $m_{avg,t}$ and $s_{avg,t}, t = 1, \dots, G$: each pixel is assigned the most popular semantic class from trainset. For each input image i at patch step t , m_t^i and s_t^i are extracted and fed to Bi-LSTM to predict $p_t^{i,for}$ and $p_t^{i,back}$. The total prediction error e_{pred} for the patch sequence is computed using methods listed in Fig.4. It is threshold-ed to determine whether in-distribution anomalies exist in the input image x_i .

4. Results and Analysis

The entire framework was implemented using the PyTorch framework [41]. The models were trained and evaluated using 4 NVIDIA GeForce GTX 2080 Ti GPU cards.

CelebA On the aligned-and-cropped CelebA [37] dataset, 202599 RGB images are resized to size 256×256 . First, we use Feature Pyramid Network (FPN) [35] with backbone on Resnet-18 [22], pre-trained on ImageNet [11] to extract $128 \times 64 \times 64$ pixel-level features (downsampled). The FPN is finetuned with 30,000 CelebAHQ [32] face part segmentation masks. We perform mini-batch K-means clustering every 20 batches before one centroid update. The number of clusters is set to 20. More deep clustering details can be found in the appendix. By merging clusters, the resulting part semantic masks contain 7 classes. For image syntax learning, a 1-layer bi-LSTM model is trained. Input and hidden vectors are 135-d (128-d encoded mask concatted with 7-d semantics), and the projected outputs are 7-d. Fig.5 shows the correct and corrupted images during the test, the 5 cropped patches in the traversal sequence, and their predicted part semantic masks.

Baseline: Bi-LSTM+next semantics The baseline method we used is described in Sec.3. In Fig.6 the left 3 sub-figures show the forward, backward, bi-directional and total prediction error (residual) across patch iterations in the part semantic sequence. The prediction error is the l_2 distance between the bi-LSTM’s prediction and the actual part semantics in a particular patch. In Fig.6 the solid lines are mean values over correct and corrupted samples, at each patch iteration; whereas the shaded region is covers between 25% and 75% percentiles. In all 3 sub-figures,

we confirm a clear separation between correct (blue) and corrupted (red) samples. The last sub-figure is the histogram plotting the distribution of total error (residual) over 5 patches for all test images. The cutoff threshold is determined from the validation set. For example, in the demonstrated scenario in Fig.5 (patch size=30, 5-patch shuffling), threshold=2.0, the binary classification accuracy is $\frac{TruePositive(TP)+TrueNegative(TN)}{FalseNegative(FN)+TP+FalsePositive(FP)+TN} = 91.72\%$. We further calculate the anomaly detection rate (recall) as $\frac{TP}{FN+TP} = 96.06\%$. We complete Table 1 covering selected corruption scenarios of shuffling, permuting, blackout, and blurring patches around 5 landmark locations [37]. We tabulate first the detection accuracy and then the ID anomaly detection rates in parentheses. For puzzle solving tasks, copies of fake patch permutations along with the correct image are simultaneously fed to our framework, and we try to pick out the single copy that has the lowest total prediction error e_{pred} . Success rate of solving the puzzle is shown.

Use of averaged semantic masks On CelebA using ResNet18+FPN segmentation, we compare the effectiveness of all 3 grammar validation methods in Fig.7a and Table 1. In the tasks of patch shuffling, blackening, and blurring, "Bi-LSTM+avg. semantics" incurs higher anomaly detection rate of 0-10% over the baseline method. This indicates that ID anomaly detection works better when comparing LSTM’s prediction to averaged part semantics instead of GT counterparts. The averaged part semantics sequence extracted from the trainset (shown in Fig.4) serve as a syntactical guideline for test patches to follow during each patch traversal. Similarly, in the task of puzzle solving, directly observing mIoU value between predicted and trainset-averaged part semantic masks results in a solving rate close to 100%. ID anomalies are easier to discern when the semantics are compared with a universal semantic representation summarized from correct samples of the object.

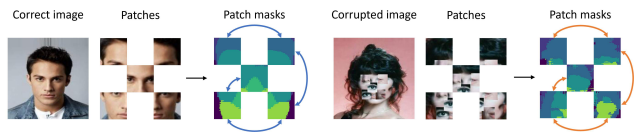


Figure 5. CelebA: sequences of image patch masks

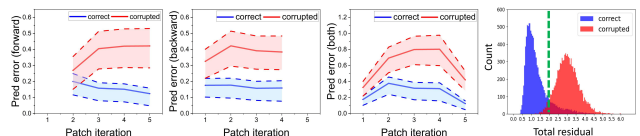


Figure 6. CelebA: forward, backward, and bi-directional LSTM prediction errors, histogram of total error (residual) over test samples (from left to right)

Dataset	Seg Model	Grammar Validation Method	Shuffle 2 20x20	Shuffle 2 30x30	Black 1 20x20	Blur 1 20x20	4 Puzzles, 20x20	4 Puzzles, 30x30
CelebA	ResNet18+FPN (ours)	Bi-LSTM + next semantics (Baseline)	65.66 (68.67)	76.22 (79.72)	70.91 (67.04)	56.53 (61.19)	86.74	92.51
CelebA	ResNet18+FPN (ours)	Bi-LSTM + avg. semantics	61.53 (71.72)	68.89 (80.48)	65.84 (72.38)	58.05 (71.50)	85.62	91.15
CelebA	ResNet18+FPN (ours)	mIoU w./ avg. semantics	60.04 (56.16)	69.59 (59.60)	60.90 (61.87)	53.69 (50.18)	99.25	99.58
CelebA	SemanticsGAN [33] (2021)	Bi-LSTM + next semantics (Baseline)	61.35 (69.87)	70.20 (73.68)	68.98 (71.04)	63.93 (65.32)	82.37	88.09
CelebA	SemanticsGAN [33] (2021)	Bi-LSTM + avg. semantics	58.26 (67.91)	63.57 (71.49)	61.28 (65.78)	59.63 (60.17)	81.23	86.79
CelebA	SemanticsGAN [33] (2021)	mIoU w./ avg. semantics	56.76 (58.34)	62.75 (64.25)	62.13 (61.87)	57.91 (58.72)	98.60	99.12

Table 1. CelebA: benchmarking grammar validation with different segmentation and test methods

Dataset	Seg Model	Grammar Validation Method	Shuffle 4 160x160	Shuffle 16 80x80	Black 4 160x160	Blur 4 160x160	4 Puzzles, 160x160	16 Puzzles, 80x80
SUN-RGBD (13-cls.)	ResNet50+Encoder-Decoder (ours)	Bi-LSTM + next semantics (Baseline)	60.57 (72.04)	76.57 (73.37)	66.55 (67.21)	55.33 (59.07)	72.89	91.17
SUN-RGBD (13-cls.)	ResNet50+Encoder-Decoder (ours)	Bi-LSTM + avg. semantics	54.97 (65.36)	61.52 (64.09)	58.46 (59.65)	52.83 (55.72)	62.47	75.48
SUN-RGBD (13-cls.)	ResNet50+Encoder-Decoder (ours)	mIoU w./ avg. semantics	57.98 (68.04)	58.98 (62.24)	56.32 (57.19)	53.38 (52.53)	97.09	98.20
SUN-RGBD (13-cls.)	Dformer-S [60] (2023)	Bi-LSTM + next semantics (Baseline)	62.16 (73.47)	74.23 (72.80)	68.86 (71.23)	59.25 (61.22)	76.61	92.84
SUN-RGBD (13-cls.)	Dformer-S [60] (2023)	Bi-LSTM + avg. semantics	53.77 (67.23)	62.45 (69.09)	61.98 (62.45)	56.22 (58.74)	61.97	74.78
SUN-RGBD (13-cls.)	Dformer-S [60] (2023)	mIoU w./ avg. semantics	53.24 (63.38)	60.46 (66.21)	59.79 (61.80)	55.67 (56.65)	98.13	98.62

Table 2. SUN-RGBD: benchmarking grammar validation with different segmentation and test methods

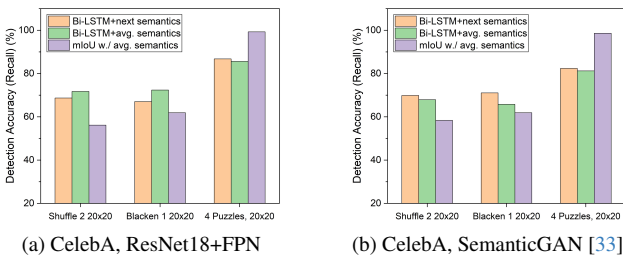


Figure 7. CelebA: comparison of detection rate by 3 test methods

Dataset	Seg Model	Seg Method	SSL?	mIoU
CelebA	ResNet18+FPN	DeepCluster [6]	✓	0.523
CelebA	SemanticGAN	StyleGAN2 [28]	✓	0.781
SUNRGBD	ResNet50	Autoencoder [27]	✗	0.498
SUNRGBD	Dformer-S	RGBD [60]	✗	0.500

Table 3. Segmentation Models

SUN-RGBD On the SUN-RGBD[46] dataset that contains 10,335 room layout RGB and depth images, we implement a pre-trained Residual Encoder-Decoder Architec-



Figure 8. SUN-RGBD (number of classes=13, patch size=160): sequences of image patch masks

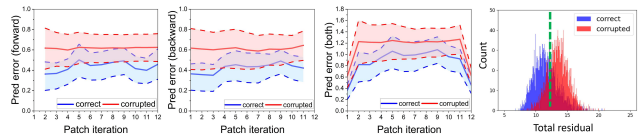


Figure 9. SUN-RGBD, patch size=160: forward, backward, and bi-directional LSTM prediction errors, histogram of total error (residual) over test samples (from left to right)

ture (RedNet)[27] to retrieve part semantic masks from 640×480 sized images. On 2 granularity levels, 37-class (appendix) and 13-class [21] semantic masks are produced. For syntax learning, we use the same bi-LSTM model as in CelebA. We define zig-zag traversal rules on sequences of patches of sizes 160 and 80. 13-class patch mask traversal with patch size 160 on correct and corrupted images is shown in Fig.8. The prediction errors and test-set histogram are shown in Fig.9. Detection accuracy and anomaly detec-

tion rates are shown in Table 2. On the coarser 13-class segmentation, the performance is marginally better.

Effect of Segmentation Granularity On both datasets, we compare a few self- and fully-supervised segmentation models that produce coarser and finer semantic masks (Table 3). From test results in Table 1, 2, we conclude that finer semantic masks don't always lead to higher ID anomaly detection rate, especially on object-centric datasets. The relationship between semantic granularity and grammar detection performance is worthy of exploring.

5. Conclusion

Motivated by the gap between human and computer vision in recognizing part corruptions in object-centric and scene-centric images, we propose a 2-stream deep learning framework that 1) extracts semantically-rich part segmentation from images through deep clustering and 2) iterates through the part semantic masks following a traversal rule to learn image syntax with respect to the object/scene class concept. We evaluate the performance of the framework in various in-distribution corruption scenarios (Table 1, 2) and achieve 70-90% part anomaly detection rate on CelebA face images and over 60-80% on SUN-RGBD room layout images. Through the novel analysis of part-level image grammar, this work tackles the challenge of in-distribution anomaly detection faced by machine vision research.

References

- [1] Paul Albert, Eric Arazo, Noel E. O’Connor, and Kevin McGuinness. Embedding contrastive unsupervised features to cluster in- and out-of-distribution noise in corrupted image datasets. In *Computer Vision – ECCV 2022: 17th European Conference, Tel Aviv, Israel, October 23–27, 2022, Proceedings, Part XXXI*, page 402–419, Berlin, Heidelberg, 2022. Springer-Verlag. 2
- [2] Yuki Markus Asano, Christian Rupprecht, and Andrea Vedaldi. Self-labelling via simultaneous clustering and representation learning. In *ICLR*. OpenReview.net, 2020. 3
- [3] Yoshua Bengio. Learning deep architectures for ai. *Found. Trends Mach. Learn.*, 2(1):1–127, 2009. 3
- [4] Yoshua Bengio, Aaron Courville, and Pascal Vincent. Representation learning: A review and new perspectives. *IEEE Trans. Pattern Anal. Mach. Intell.*, 35(8):1798–1828, 2013. 3
- [5] Stefano F. Cappa. Imaging semantics and syntax. *NeuroImage*, 61(2):427–431, 2012. NEUROIMAGING: THEN, NOW AND THE FUTURE. 2
- [6] Mathilde Caron, Piotr Bojanowski, Armand Joulin, and Matthijs Douze. Deep clustering for unsupervised learning of visual features. In *Proceedings of the European Conference on Computer Vision (ECCV)*, 2018. 2, 3, 4, 8
- [7] Mathilde Caron, Hugo Touvron, Ishan Misra, Hervé Jégou, Julien Mairal, Piotr Bojanowski, and Armand Joulin. Emerging properties in self-supervised vision transformers, 2021. 3
- [8] Varun Chandola, Arindam Banerjee, and Vipin Kumar. Anomaly detection: A survey. *ACM Comput. Surv.*, 41(3), 2009. 2
- [9] Jang Hyun Cho, Utkarsh Mall, Kavita Bala, and Bharath Hariharan. Picie: Unsupervised semantic segmentation using invariance and equivariance in clustering. In *Proceedings of the IEEE/CVF Conference on Computer Vision and Pattern Recognition (CVPR)*, pages 16794–16804, 2021. 2, 3, 4, 5, 1
- [10] Junsuk Choe, Seong Joon Oh, Seung-ho Lee, Sanghyuk Chun, Zeynep Akata, and Hyunjung Shim. Evaluating weakly supervised object localization methods right. In *CVPR*, pages 3130–3139. IEEE, 2020. 4
- [11] Jia Deng, Wei Dong, Richard Socher, Li-Jia Li, Kai Li, and Li Fei-Fei. Imagenet: A large-scale hierarchical image database. In *2009 IEEE conference on computer vision and pattern recognition*, pages 248–255. Ieee, 2009. 2, 7
- [12] Alexey Dosovitskiy, Lucas Beyer, Alexander Kolesnikov, Dirk Weissenborn, Xiaohua Zhai, Thomas Unterthiner, Mostafa Dehghani, Matthias Minderer, Georg Heigold, Sylvain Gelly, Jakob Uszkoreit, and Neil Houlsby. An image is worth 16x16 words: Transformers for image recognition at scale. *CoRR*, abs/2010.11929, 2020. 3
- [13] Alexey Dosovitskiy, Lucas Beyer, Alexander Kolesnikov, Dirk Weissenborn, Xiaohua Zhai, Thomas Unterthiner, Mostafa Dehghani, Matthias Minderer, Georg Heigold, Sylvain Gelly, Jakob Uszkoreit, and Neil Houlsby. An image is worth 16x16 words: Transformers for image recognition at scale. *ICLR*, 2021. 2
- [14] Soumya Suvra Ghosal, Yifei Ming, and Yixuan Li. Are vision transformers robust to spurious correlations?, 2022. 2
- [15] Jean-Bastien Grill, Florian Strub, Florent Alché, Corentin Tallec, Pierre H. Richemond, Elena Buchatskaya, Carl Doersch, Bernardo Avila Pires, Zhaohan Daniel Guo, Mohammad Gheshlaghi Azar, Bilal Piot, Koray Kavukcuoglu, Rémi Munos, and Michal Valko. Bootstrap your own latent a new approach to self-supervised learning. In *Proceedings of the 34th International Conference on Neural Information Processing Systems*, Red Hook, NY, USA, 2020. Curran Associates Inc. 3
- [16] Jindong Gu, Volker Tresp, and Yao Qin. Are vision transformers robust to patch perturbations?, 2022. 3
- [17] THOMAS C. GUNTER, LAURIE A. STOWE, and GUSBERTUS MULDER. When syntax meets semantics. *Psychophysiology*, 34(6):660–676, 1997. 2
- [18] Xifeng Guo, Xinwang Liu, En Zhu, and Jianping Yin. Deep clustering with convolutional autoencoders. In *ICONIP (2)*, pages 373–382. Springer, 2017. 3
- [19] Yong Guo, David Stutz, and Bernt Schiele. Improving robustness of vision transformers by reducing sensitivity to patch corruptions. In *Proceedings of the IEEE/CVF Conference on Computer Vision and Pattern Recognition (CVPR)*, pages 4108–4118, 2023. 3
- [20] Mark Hamilton, Zhoutong Zhang, Bharath Hariharan, Noah Snavely, and William T. Freeman. Unsupervised semantic segmentation by distilling feature correspondences, 2022. 3
- [21] Ankur Handa, Viorica Pătrăucean, Simon Stent, and Roberto Cipolla. Scenenet: an annotated model generator for indoor scene understanding. In *ICRA*, 2016. 8, 2
- [22] Kaiming He, Xiangyu Zhang, Shaoqing Ren, and Jian Sun. Deep residual learning for image recognition. In *2016 IEEE Conference on Computer Vision and Pattern Recognition (CVPR)*, pages 770–778, 2016. 2, 3, 7, 1
- [23] Kaiming He, Haoqi Fan, Yuxin Wu, Saining Xie, and Ross Girshick. Momentum contrast for unsupervised visual representation learning, 2019. cite arxiv:1911.05722Comment: CVPR 2020 camera-ready. Code: <https://github.com/facebookresearch/moco>. 3
- [24] Yuansheng Hua, Lichao Mou, and Xiao Xiang Zhu. Lahnet: A convolutional neural network fusing low- and high-level features for aerial scene classification. In *IGARSS 2018 - 2018 IEEE International Geoscience and Remote Sensing Symposium*, pages 4728–4731, 2018. 2
- [25] Timur Ibrayev, Manish Nagaraj, Amitangshu Mukherjee, and Kaushik Roy. Exploring foveation and saccade for improved weakly-supervised localization. In *NeurIPS 2023 Workshop on Gaze Meets ML*, 2023. 4
- [26] Xu Ji, Andrea Vedaldi, and João F. Henriques. Invariant information clustering for unsupervised image classification and segmentation. In *ICCV*, pages 9864–9873. IEEE, 2019. 3
- [27] Jindong Jiang, Lunan Zheng, Fei Luo, and Zhijun Zhang. Rednet: Residual encoder-decoder network for indoor rgb-d semantic segmentation. *arXiv preprint arXiv:1806.01054*, 2018. 8, 1, 2

- [28] Tero Karras, Samuli Laine, Miika Aittala, Janne Hellsten, Jaakko Lehtinen, and Timo Aila. Analyzing and improving the image quality of StyleGAN. In *Proc. CVPR*, 2020. 8
- [29] Aditya Khosla, Nityananda Jayadevaprakash, Bangpeng Yao, and Li Fei-Fei. Novel dataset for fine-grained image categorization. In *First Workshop on Fine-Grained Visual Categorization, IEEE Conference on Computer Vision and Pattern Recognition*, Colorado Springs, CO, 2011. 2
- [30] Alexander Kirillov, Ross B. Girshick, Kaiming He, and Piotr Dollár. Panoptic feature pyramid networks. In *CVPR*, pages 6399–6408. Computer Vision Foundation / IEEE, 2019. 1
- [31] Alex Krizhevsky, Ilya Sutskever, and Geoffrey E Hinton. Imagenet classification with deep convolutional neural networks. In *Advances in neural information processing systems*, pages 1097–1105, 2012. 2, 3
- [32] Cheng-Han Lee, Ziwei Liu, Lingyun Wu, and Ping Luo. Maskgan: Towards diverse and interactive facial image manipulation. In *IEEE Conference on Computer Vision and Pattern Recognition (CVPR)*, 2020. 3, 7, 2
- [33] Daiqing Li, Junlin Yang, Karsten Kreis, Antonio Torralba, and Sanja Fidler. Semantic segmentation with generative models: Semi-supervised learning and strong out-of-domain generalization. In *Conference on Computer Vision and Pattern Recognition (CVPR)*, 2021. 8
- [34] Kunchang Li, Yali Wang, Peng Gao, Guanglu Song, Yu Liu, Hongsheng Li, and Yu Qiao. Uniformer: Unified transformer for efficient spatiotemporal representation learning. *CoRR*, abs/2201.04676, 2022. 3
- [35] Tsung-Yi Lin, Piotr Dollár, Ross B. Girshick, Kaiming He, Bharath Hariharan, and Serge J. Belongie. Feature pyramid networks for object detection. In *CVPR*, pages 936–944. IEEE Computer Society, 2017. 7, 1
- [36] Chenxi Liu, Zhe Lin, Xiaohui Shen, Jimei Yang, Xin Lu, and Alan L. Yuille. Recurrent multimodal interaction for referring image segmentation. In *ICCV*, pages 1280–1289. IEEE Computer Society, 2017. 3
- [37] Ziwei Liu, Ping Luo, Xiaogang Wang, and Xiaoou Tang. Deep learning face attributes in the wild. In *Proceedings of International Conference on Computer Vision (ICCV)*, 2015. 7, 1, 2
- [38] Ze Liu, Yutong Lin, Yue Cao, Han Hu, Yixuan Wei, Zheng Zhang, Stephen Lin, and Baining Guo. Swin transformer: Hierarchical vision transformer using shifted windows. *2021 IEEE/CVF International Conference on Computer Vision (ICCV)*, pages 9992–10002, 2021. 2, 3
- [39] Volodymyr Mnih, Nicolas Heess, Alex Graves, and Koray Kavukcuoglu. Recurrent models of visual attention. In *NIPS*, pages 2204–2212, 2014. 3
- [40] Diego Ortego, Eric Arazo, Paul Albert, Noel E. O’Connor, and Kevin McGuinness. Towards robust learning with different label noise distributions. In *2020 25th International Conference on Pattern Recognition (ICPR)*, pages 7020–7027, 2021. 2
- [41] Adam Paszke, Sam Gross, Francisco Massa, Adam Lerer, James Bradbury, Gregory Chanan, Trevor Killeen, Zeming Lin, Natalia Gimelshein, Luca Antiga, Alban Desmaison, Andreas Kopf, Edward Yang, Zachary DeVito, Martin Raison, Alykhan Tejani, Sasank Chilamkurthy, Benoit Steiner, Lu Fang, Junjie Bai, and Soumith Chintala. Pytorch: An imperative style, high-performance deep learning library. In *Advances in Neural Information Processing Systems 32*, pages 8024–8035. Curran Associates, Inc., 2019. 7
- [42] Sudipan Saha, Muhammad Shahzad, Lichao Mou, Qian Song, and Xiao Xiang Zhu. Unsupervised single-scene semantic segmentation for earth observation. *IEEE Transactions on Geoscience and Remote Sensing*, 60:1–11, 2022. 3
- [43] Raimondo Schettini, Gianluigi Ciocca, and Isabella Gagliardi. *Feature Extraction for Content-Based Image Retrieval*, pages 1115–1119. Springer US, Boston, MA, 2009. 2
- [44] Zong-Ying Shen, Shiang-Yu Han, Li-Chen Fu, Pei-Yung Hsiao, Yo-Chung Lau, and Sheng-Jen Chang. Deep convolution neural network with scene-centric and object-centric information for object detection. *Image and Vision Computing*, 85:14–25, 2019. 2
- [45] Karen Simonyan and Andrew Zisserman. Very deep convolutional networks for large-scale image recognition. In *ICLR*, 2015. 2, 3
- [46] Shuran Song, Samuel P. Lichtenberg, and Jianxiong Xiao. Sun rgb-d: A rgb-d scene understanding benchmark suite. In *CVPR*, pages 567–576. IEEE Computer Society, 2015. 8, 1, 2
- [47] Andreas Peter Steiner, Alexander Kolesnikov, Xiaohua Zhai, Ross Wightman, Jakob Uszkoreit, and Lucas Beyer. How to train your vit? data, augmentation, and regularization in vision transformers. *Transactions on Machine Learning Research*, 2022. 2
- [48] Rui Tian, Zuxuan Wu, Qi Dai, Han Hu, and Yu-Gang Jiang. Deeper insights into the robustness of vits towards common corruptions, 2022. 3
- [49] Wouter Van Gansbeke, Simon Vandenhende, Stamatios Georgoulis, and Luc Van Gool. Unsupervised semantic segmentation by contrasting object mask proposals. In *Proceedings of the IEEE/CVF International Conference on Computer Vision (ICCV)*, pages 10052–10062, 2021. 3
- [50] Arnim von Stechow. Syntax and semantics: an overview. *Semantics-Interfaces*, page 169, 2019. 2
- [51] Guangrun Wang, Yansong Tang, Liang Lin, and Philip H.S. Torr. Semantic-aware auto-encoders for self-supervised representation learning. In *Proceedings of the IEEE/CVF Conference on Computer Vision and Pattern Recognition (CVPR)*, pages 9664–9675, 2022. 3
- [52] Hua Wang, Feiping Nie, and Heng Huang. Multi-view clustering and feature learning via structured sparsity. In *Proceedings of the 30th International Conference on Machine Learning*, pages 352–360, Atlanta, Georgia, USA, 2013. PMLR. 3
- [53] Mike Wu, Milan Mosse, Chengxu Zhuang, Daniel Yamins, and Noah D. Goodman. Conditional negative sampling for contrastive learning of visual representations. *CoRR*, abs/2010.02037, 2020. 3
- [54] Zhi-Fan Wu, Tong Wei, Jianwen Jiang, Chaojie Mao, Mingqian Tang, and Yu-Feng Li. Ngc: A unified framework for learning with open-world noisy data. In *Proceedings of the IEEE/CVF International Conference on Computer Vision*, pages 62–71, 2021. 2

- [55] Xuan Xia, Xizhou Pan, Nan Li, Xing He, Lin Ma, Xiaoguang Zhang, and Ning Ding. Gan-based anomaly detection: A review. *Neurocomput.*, 493(C):497–535, 2022. 2
- [56] Junyuan Xie, Ross B. Girshick, and Ali Farhadi. Unsupervised deep embedding for clustering analysis. In *ICML*, pages 478–487. JMLR.org, 2016. 3
- [57] Kelvin Xu, Jimmy Ba, Ryan Kiros, Kyunghyun Cho, Aaron Courville, Ruslan Salakhudinov, Rich Zemel, and Yoshua Bengio. Show, attend and tell: Neural image caption generation with visual attention. In *Proceedings of the 32nd International Conference on Machine Learning*, pages 2048–2057, Lille, France, 2015. PMLR. 3
- [58] Minghao Xu, Yuanfan Guo, Xuanyu Zhu, Jiawen Li, Zhenbang Sun, Jian Tang, Yi Xu, and Bingbing Ni. Hirl: A general framework for hierarchical image representation learning, 2022. 3
- [59] Jianwei Yang, Devi Parikh, and Dhruv Batra. Joint unsupervised learning of deep representations and image clusters. In *CVPR*, pages 5147–5156. IEEE Computer Society, 2016. 3
- [60] Bowen Yin, Xuying Zhang, Zhongyu Li, Li Liu, Ming-Ming Cheng, and Qibin Hou. Dformer: Rethinking rgb-d representation learning for semantic segmentation. *arXiv preprint arXiv:2309.09668*, 2023. 8
- [61] Sukmin Yun, Hankook Lee, Jaehyung Kim, and Jinwoo Shin. Patch-level representation learning for self-supervised vision transformers. In *Proceedings of the IEEE/CVF Conference on Computer Vision and Pattern Recognition (CVPR)*, pages 8354–8363, 2022. 3
- [62] Xiaohang Zhan, Jiahao Xie, Ziwei Liu, Yew-Soon Ong, and Chen Change Loy. Online deep clustering for unsupervised representation learning. In *CVPR*, pages 6687–6696. IEEE, 2020. 3
- [63] Chiyuan Zhang, Samy Bengio, Moritz Hardt, Benjamin Recht, and Oriol Vinyals. Understanding deep learning (still) requires rethinking generalization. *Commun. ACM*, 64(3): 107–115, 2021. 2
- [64] Richard Zhang. Making convolutional networks shift-invariant again. In *Proceedings of the 36th International Conference on Machine Learning*, pages 7324–7334. PMLR, 2019. 3
- [65] Daquan Zhou, Zhiding Yu, Enze Xie, Chaowei Xiao, Animesh Anandkumar, Jiashi Feng, and Jose M. Alvarez. Understanding the robustness in vision transformers. In *Proceedings of the 39th International Conference on Machine Learning*, pages 27378–27394. PMLR, 2022. 2

Towards Image Semantics and Syntax Sequence Learning

Supplementary Material

6. Experiment details

6.1. DNN architectures

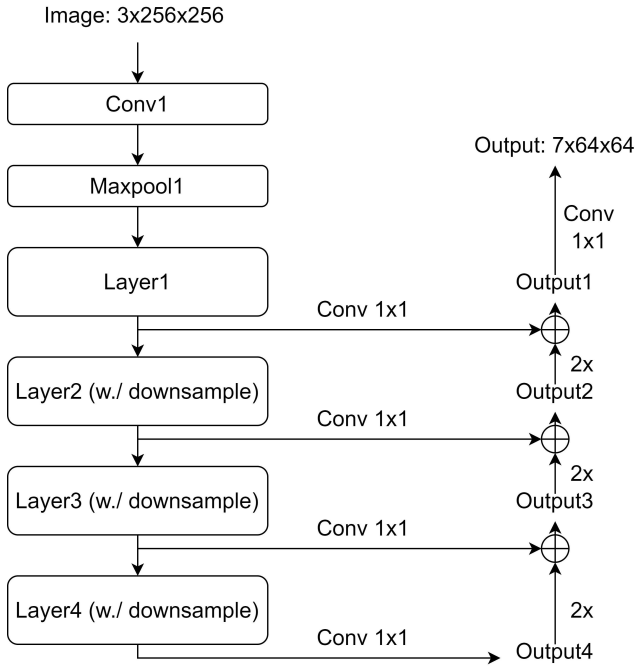


Figure 10. DNN architectures: Feature Pyramid Network (FPN) backbone on ResNet-18

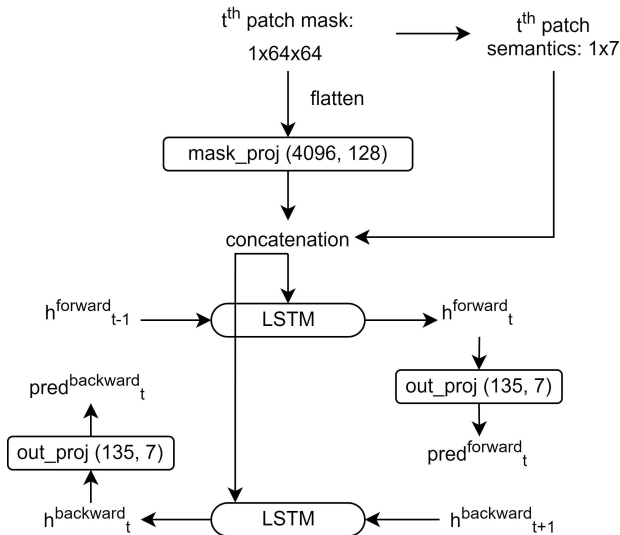


Figure 11. DNN architectures: bi-directional Long Short-Term Memory (bi-LSTM)

On CelebA In Fig.10 we illustrate the feature pyramid network (FPN) [35] that we used for part semantics clustering and segmentation of CelebA [37] images. The Panoptic FPN [30] we used is backbone on ResNet-18 [22]. It encodes multi-scale feature representation in a top-down fashion. Then from the bottom-up, we use 1×1 Convolutional (Conv) layers to project pixel-wise features to 128-dimensional. The projected features of different spatial sizes are bilinearly-upsampled to $1/4$ height and width of the original image and then element-wise summed. The pixel-wise representations thus have shape $128 \times h \times w$ ($128 \times 64 \times 64$ for input images of shape $3 \times 256 \times 256$). The extracted pixel-wise features are used for the DeepClustering method [9]. We record the resulting clustering centroids as a final 1×1 Conv layer to project these features to the dimension of the number of semantic classes, 7 in the case of face images.

In Fig.11 is the structure of the bi-directional Long Short-Term Memory (bi-LSTM). We use it for image syntax learning. For each patch in the traversal sequence of length 5, the predicted mask is first flattened before being fed to a fully-connected (FC) encoder layer. The encoder projects the semantic mask to a 128-d vector, which is concatenated with the 7-d semantics vector. The resulting 135-d vector contains both spatial and semantic information about each patch's composition, and it is used as the input to 2 LSTM layers in forward and backward directions. After projection layers, the outputs include a 7-d forward prediction of the next semantics in the sequence and a 7-d backward prediction of the previous semantics. For the first and last patches, only forward and backward predictions are made, respectively.

On SUN-RGBD We use a Residual Encoder-Decoder Network (RedNet) [27] with backbone on ResNet-50 for segmentation on SUN-RGBD [46] images. It is a state-of-the-art room scene parsing architecture that achieved 47.8% mIoU accuracy on 37-class SUN-RGBD. Similar to FPN, the RedNet extracts multi-scale feature maps from the input image with its encoder residual layers. However, each projected feature map is skip-connected with the output of upsampling residual units in a decoder [27] before being summed with the next level in the feature pyramid. An additional depth branch is fused with the RGB branch. We performed 13-class (merged from 37-class) semantic segmentation with a trained RedNet. The RedNet produces the same-resolution (640×480) segmentation from the original image. Patch semantic masks of sizes 160×160 and 80×80 are cropped and used for preparing patch semantic

vectors. At each stage of patch sequences, patch semantic masks are flattened and projected to 128-d vectors before concatenating with a 13-d semantics vector. The resulting 141-d vectors are passed to LSTM blocks for forward and backward predictions (both 13-d).

6.2. Datasets

Label	Class name
6	Background
5	Hair
4	Forehead
3	Eyes
2	Nose
1	Mouth
0	Neck

Label	Class name	Label	Class name
1	Bed	8	Picture
2	Books	9	Sofa
3	Ceiling	10	Table
4	Chair	11	TV
5	Floor	12	Walls
6	Furniture	13	Window
7	Objects		

Figure 12. Segmentation Classes. Left: CelebA; Right: SUN-RGBD

CelebA [37] contains 202,599 celebrity images. We used the aligned-and-cropped version where faces are localized. Images are divided into a train set of size 162,770, a validation set of size 19,867, and a test set of size 19,962. First, the FPN network is finetuned on 30,000 CelebAHQ [32] images selected from CelebA. CelebAHQ images and pixel-wise labels are center-cropped (size=160) and resized to 256×256 . After fine-tuning, DeepCluster PiCIE [9] training is accomplished on train set images resized to 256×256 and validated on the validation set. 64×64 patches are cropped from segmentation and are bi-linearly-interpolated to 256×256 . The part mask detector again produces 64×64 patch semantic masks. The 7 semantic classes and their names are illustrated in Fig.12 on the left. During the test, we add corruption to half of the test images around 5 facial part landmark locations (left eye, right eye, nose, left mouth, right mouth).

SUN-RGBD [46] contains 10335 RGB images and corresponding depth images, split into a train set of size 4785, a validation set of size 1000, and a test set of size 5050. RGB and depth images are resized to 640×480 and normalized. The pre-trained RedNet [27] also produces 640×480 semantic masks. From each segmentation, 160×160 and 80×80 patch semantic masks are cropped. The segmentation contains 37 semantic classes, but we merge them into 13 classes with the same mapping in [21]. The 13 semantic classes are shown in Fig.12 on the right. During the test, we add corruptions to image patches.

6.3. Train and test configurations

On CelebA During fine-tuning of the FPN network pre-trained on ImageNet [11], CelebAHQ [32] masks are pre-processed to contain only 7 coarse semantic classes. $batch_size_train = 128$. Adam optimizer is used with $start_lr = 1e^{-4}$. We trained for $num_epochs = 20$ with a constant learning rate. The fine-tuned model is used for

DeepCluster PiCIE [9] training. $batch_size_train = 256$. We adopted over-clustering and set the number of clusters, $K_train = 20$, as that results in better clusters compared to $KM_num = 10$ and $KM_num = 30$. Mini-batch K-means clustering is performed. $KM_init = 20$ is the number of batches we collect before the first K-means clustering. $KM_num = 20$ is the interval of batches between consecutive clustering. $KM_iter = 100$ is the number of K-means clustering iterations before convergence. After each clustering, the total PiCIE loss is back-propagated to optimize FPN model parameters. We use Adam optimizer with $start_lr = 1e^{-4}$. Although PiCIE loss is computing-intensive, PiCIE training converges fast in $num_epochs = 10$ with a constant learning rate. To get semantic segmentation masks, we initiate a 1×1 Conv layer whose weights are loaded as the trained centroid matrix, and append it to the trained FPN network. $batch_size_test = 256$. We post-process pixel-wise class assignments to merge semantically-similar clusters and obtain 7-class face part masks. Further, we tune the FPN network on 64×64 patches, using crops on the saved face masks as supervision. The part mask detector is trained with $batch_size_train = 128$, $start_lr = 1e^{-4}$, and $num_epochs = 20$. We chose the $num_epochs = 20$ model over the $num_epochs = 40$ model because the smooth boundaries in the semantic masks help with syntax learning.

After we obtain 7-class patch semantic masks for each patch in the traversal sequence, we feed the concatenation of encoded mask (128-d) and semantics vector (7-d) into a bi-LSTM model. $input_size = 135$, $hidden_size = 135$, $num_layers = 1$, $bidirectional = True$, $proj_size = 7$. We use Adam optimizer with $start_lr = 1e^{-4}$. $num_epochs = 40$ and the learning rate changes to $1e^{-5}$ after 20 epochs. During the test, we apply the same settings to the bi-LSTM model and use a threshold on total prediction error to distinguish part semantic anomalies in patch sequences.

On SUN-RGBD On SUN-RGBD, the pre-trained RedNet network [27] produces 37 segmentation classes. We merge these classes into 13-class stuff and things as shown in Fig.12. When the patches are shuffled, the pre-trained network is able to produce precise patch semantics, so that a part mask detector is not needed as in CelebA. We start with image syntax training with two configurations, $patch_size = 160$ and $patch_size = 80$. In both configurations, the patch semantic masks are encoded as 128-d vectors, while the semantics vector is 13-d. Thus, the bi-LSTM model has configurations $input_size = 141$, $hidden_size = 141$, $num_layers = 1$, $bidirectional = True$, $proj_size = 13$. We use Adam optimizer with $start_lr = 1e^{-4}$. $num_epochs = 40$. A multi-step

learning rate scheduler is used with $\gamma = 0.8$ and $\text{milestones} = [5, 10, 15, 20, 25, 30, 35]$. Same bi-LSTM model is used during test.

7. Quantitative results

In Table 4 and 5 we add more results for the task of in-distribution anomaly detection, on CelebA (7 classes) and SUN-RGBD (13 classes), respectively.

CelebA The segmentation model is ResNet18+FPN. The input images have sizes 256×256 . All results are reported using the baseline test method "Bi-LSTM+next semantics". From Table 4, we observe that the grammar detection framework exhibits reliable performance when the size of the corrupted patch exceeds 30×30 : $\approx 80\%$ on patch shuffling tasks, 92.51% on puzzle solving with 4 permutations, $\approx 80\%$ on patch blackout tasks, and $\approx 60\%$ on patch blurring tasks.

SUN-RGBD The segmentation model is ResNet50 encoder-decoder (RedNet). The input images have sizes 640×480 . All results are reported using the baseline test method "Bi-LSTM+next semantics". Two segmentation granularities are used, 13-class coarse segmentation merged from 37-classes, and the original 37-class fine segmentation. From Table 5, we observe corruption detection performance for the two levels of granularity. In tasks such as patch shuffling, puzzle solving, and patch blurring, using coarser 13-class semantic masks boosts syntax sequence reasoning and improves grammar validation performance. This is due to the better sequential reasoning capability that the Bi-LSTM learns from coarse patch masks. Meanwhile, in the task of patch blackout, using finer 37-class semantic masks has an edge. The blackened patch semantics is easier to discern when the segmentation is finer, leading to a longer syntax sequence and higher variations in the predicted semantic values.

8. Qualitative results

8.1. Semantic clustering and segmentation

In the below Fig.13 and Fig.14 we show selected part-level semantic segmentations on CelebA face images and SUN-RGBD room scene images, respectively. All samples are in the trainsets. The segmentations displayed by generated by trained ResNet18 and trained ResNet50 encoder-decoder, respectively.

8.2. Syntactic sequences of part semantics

In Fig.15 we show the pixel-level part semantic masks and explicit semantics in each mask, averaged over correct samples in the entire CelebA test set. During training, we op-

timized MSE loss between bi-LSTM predictions and the actual semantics inside each patch, in order to model the mean of the semantics distribution in each patch iteration, as discussed in the method Section. Hence, here we show the average traversal patterns learned. It's evidently shown that face-part semantic transitions and the face syntax in the CelebA dataset are captured by the trained bi-LSTM model. For example, in the first 2 patch iterations, the "forehead" semantics is dominant. In the third and fourth patches, "mouth" semantics is dominant. While for the last patch, "eyes" semantics is dominant. These part semantics along with transitions among those semantics is key to identifying part anomalies.

In Fig.16 we show the pixel-level part semantic masks and explicit semantics in each mask, averaged over the entire SUN-RGBD test set. Here, each of the 13 semantic classes is either a stuff (e.g., ceiling, floor, wall, etc.) or a thing (e.g., books, chair, table, etc.) Within the traversal sequence, the first few patches at the top of the image have "wall" as dominant semantics, while the last few patches at the bottom have "floor" as dominant. Semantic classes belonging to the thing category reside in the middle patches, such as "chair" and "table". This reveals that our proposed framework is capable of learning general stuff and thing layouts even from a complicated dataset SUN-RGBD, that contains a wide variety of different room scenes.

8.3. Corruption scenarios

In Fig.17 we made visualizations for all corruption scenarios on CelebA and SUN-RGBD test images.

9. Image corruption algorithms

In Fig.18 and Fig.19 we display the algorithms we used to generate corruptions to test images.

10. Additional results

10.1. SUN-RGBD, patch size=80

Fig.20, Fig.21, and Fig.22 are a continuation to Fig.8 that shows the demonstrations of correct and corrupted image patch traversals and the prediction errors across patch sequences, for $\text{patch_size} = 80$ traversals on 640×480 SUN-RGBD images. In Fig.22, the red and blue solid lines are mean values over all correct and corrupted samples, at each patch iteration. The dashed lines are 25% and 75% percentiles. It is noted among each row of patches, the prediction error gradually decreases, before rising again at the corner patch in the zig-zagging traversal. Thus, each row of patches can be deemed as a sub-sequence where sub-image level syntax can be learned.

Corruption: landmark shuffling					
Test Accuracy (%)	Patch size: 10	Patch size: 20	Patch size: 30	Patch size: 40	Patch size:50
shuffle 2 patches	53.86 (75.58)	65.66 (68.67)	76.22 (79.72)	83.89 (86.33)	88.22 (93.04)
shuffle 3 patches	55.67 (75.16)	73.16 (78.97)	85.68 (91.08)	90.96 (95.22)	93.05 (97.42)
shuffle 4 patches	57.33 (74.73)	78.40 (82.29)	89.79 (94.57)	93.00 (97.34)	94.34 (98.07)
shuffle 5 patches	59.13 (70.93)	82.88 (88.15)	91.72 (96.06)	93.93 (97.25)	94.69 (97.39)
Corruption: landmark puzzle					
Test Accuracy (%)	Patch size: 10	Patch size: 20	Patch size: 30	Patch size: 40	Patch size:50
1 real, 3 fake	57.84	86.74	92.51	93.97	94.81
1 real, 119 fake (all perm)	8.39	37.43	66.15	80.37	87.23
Corruption: landmark blackout					
Test Accuracy (%)	Patch size: 10	Patch size: 20	Patch size: 30	Patch size: 40	Patch size:50
blacken 1 patch	54.73 (55.36)	70.91 (67.04)	81.25 (81.08)	87.37 (88.04)	91.25 (95.12)
blacken 2 patches	60.43 (63.78)	83.83 (85.22)	91.77 (93.43)	95.41 (97.41)	95.78 (97.58)
blacken 3 patches	65.79 (68.94)	90.60 (93.83)	96.48 (98.49)	97.83 (98.57)	98.50 (99.14)
blacken 4 patches	71.85 (74.34)	94.56 (97.14)	98.08 (98.88)	98.86 (99.36)	99.05 (99.49)
blacken 5 patches	77.32 (85.28)	97.22 (98.20)	98.87 (99.48)	98.95 (99.29)	99.13 (99.64)
Corruption: landmark blurring					
Test Accuracy (%)	Patch size: 10	Patch size: 20	Patch size: 30	Patch size: 40	Patch size:50
blur 1 patch	52.31 (80.28)	56.84 (56.31)	62.12 (64.41)	66.83 (66.33)	72.64 (77.95)
blur 2 patches	54.00 (71.81)	63.21 (63.78)	72.47 (77.61)	78.53 (80.87)	83.09 (89.99)
blur 3 patches	55.88 (64.42)	69.40 (71.47)	81.03 (84.44)	86.92 (90.42)	89.66 (92.61)
blur 4 patches	57.44 (78.69)	74.61 (81.90)	87.89 (92.37)	91.32 (95.27)	92.85 (97.04)
blur 5 patches	59.65 (65.18)	78.75 (84.54)	91.34 (95.98)	93.02 (97.36)	94.03 (97.46)

Table 4. Grammar validation accuracy on CelebA (Image size: 256x256)

(a) 13 segmentation classes				(b) 37 segmentation classes			
Corruption: patch shuffling				Corruption: patch shuffling			
Test Accuracy (%)	Patch size: 160	Test Accuracy (%)	Patch size: 80	Test Accuracy (%)	Patch size: 160	Test Accuracy (%)	Patch size: 80
shuffle 4 patches	60.57 (72.04)	shuffle 16 patches	76.57 (73.37)	shuffle 4 patches	62.32 (74.57)	shuffle 16 patches	67.74 (74.77)
shuffle 8 patches	69.31 (72.59)	shuffle 32 patches	86.63 (82.38)	shuffle 8 patches	71.53 (76.99)	shuffle 32 patches	78.04 (76.20)
shuffle 12 patches	73.47 (77.50)	shuffle 48 patches	87.09 (82.97)	shuffle 12 patches	74.93 (77.43)	shuffle 48 patches	79.84 (78.69)
Corruption: patch puzzle				Corruption: patch puzzle			
Test Accuracy (%)	Patch size: 160	Test Accuracy (%)	Patch Size: 80	Test Accuracy (%)	Patch size: 160	Test Accuracy (%)	Patch Size: 80
1 real, 3 fake	72.89	1 real, 3 fake	91.17	1 real, 3 fake	76.10	1 real, 3 fake	81.23
1 real, 99 fake	28.95	1 real, 99 fake	69.67	1 real, 99 fake	33.85	1 real, 99 fake	55.99
Corruption: patch blackout				Corruption: patch blackout			
Test Accuracy (%)	Patch size: 160	Test Accuracy (%)	Patch size: 80	Test Accuracy (%)	Patch size: 160	Test Accuracy (%)	Patch size: 80
blacken 4 patches	66.55 (67.21)	blacken 16 patches	67.43 (65.53)	blacken 4 patches	61.58 (71.37)	blacken 16 patches	61.41 (71.25)
blacken 8 patches	66.59 (67.17)	blacken 32 patches	75.68 (70.22)	blacken 8 patches	67.53 (72.20)	blacken 32 patches	69.07 (71.80)
blacken 12 patches	66.75 (67.49)	blacken 48 patches	73.66 (74.81)	blacken 12 patches	66.18 (76.00)	blacken 48 patches	64.59 (72.24)
Corruption: patch blurring				Corruption: patch blurring			
Test Accuracy (%)	Patch size: 160	Test Accuracy (%)	Patch size: 80	Test Accuracy (%)	Patch size: 160	Test Accuracy (%)	Patch size: 80
blur 4 patches	55.33 (59.07)	blur 16 patches	54.42 (63.37)	blur 4 patches	54.00 (52.81)	blur 16 patches	50.91 (54.10)
blur 6 patches	56.57 (70.22)	blur 24 patches	55.42 (65.58)	blur 6 patches	54.06 (58.81)	blur 24 patches	52.88 (57.15)

Table 5. Grammar validation accuracy on SUN-RGBD (Image size: 640x480)

11. Broader impacts

This work focuses on understanding part-level image grammar and using that knowledge to detect in-distribution part anomalies inside images. With the development of a computer vision system that is more intelligent and less error-prone, people, particularly those with mental or physical disabilities and the elderly, will be able to perceive the sur-

rounding scene and objects with greater accuracy and with a lesser degree of effort. For instance, cabin vision systems can recognize dangerous behaviors by the drivers; home robots equipped with such vision systems will recognize home objects and perform housework more effectively, etc. In addition, the ability to detect part anomalies provides an additional level of defense against malicious actors trying

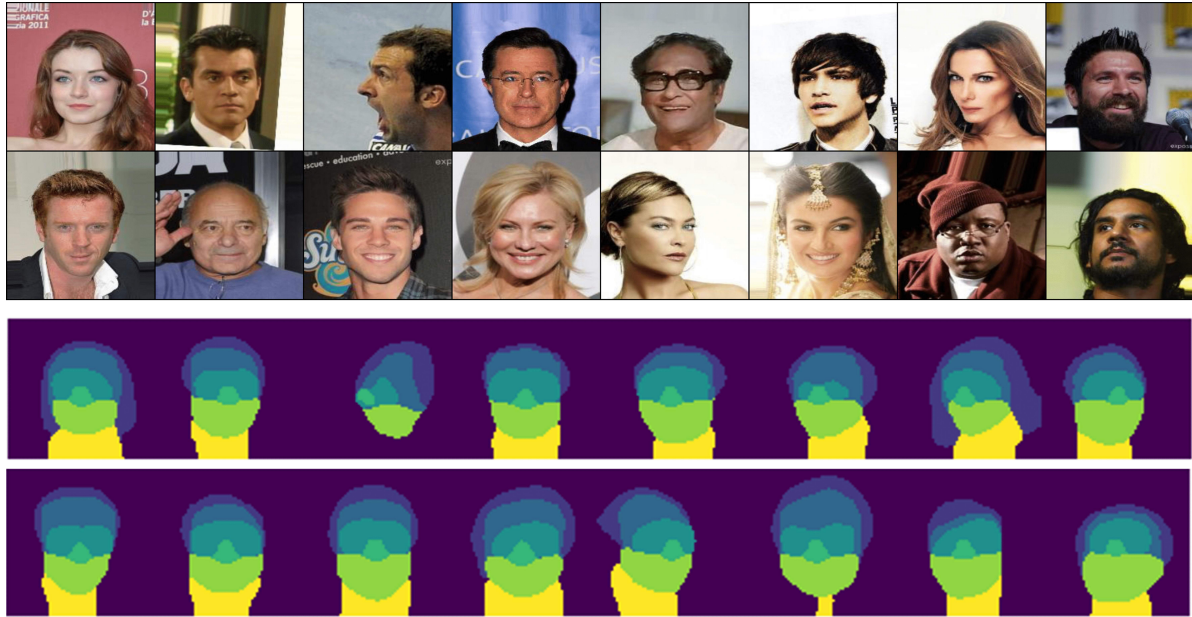


Figure 13. 7-class semantic segmentation on CelebA

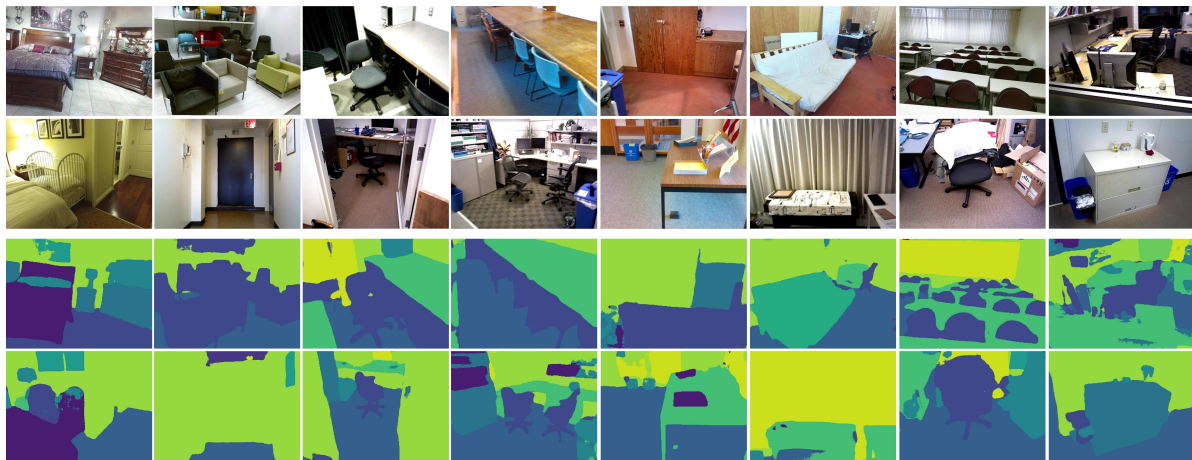


Figure 14. 13-class semantic segmentation on SUN-RGBD

to deceive modern-day machine vision algorithms. With a more powerful object perception, computer vision is more versatile in serving humans and adds convenience to everyday life.

However, we must be wary of the potential negative social consequences caused by the sophistication of machine vision. One example is where mass data sets for machine vision training can lead to information leaks and privacy issues. It would be difficult to verify the source of the information. In addition, people may improperly use high-performance machine systems for malicious purposes, such as mass surveillance and cyber warfare. Finally, it is possible that these machine vision systems are too trusted and

put to applications too soon without enough trial-and-error. In the event that these systems fail in the real world, such acts could result in serious accidents.

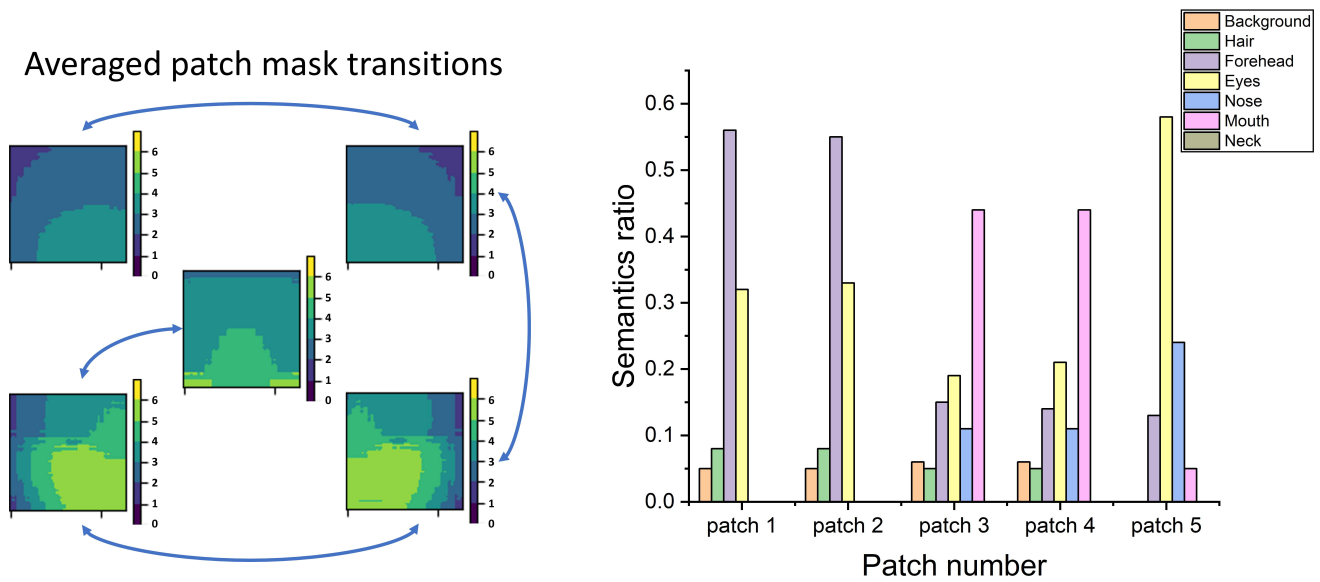


Figure 15. Left: Averaged patch mask transitions over CelebA test set; Right: Averaged patch semantics over CelebA test set

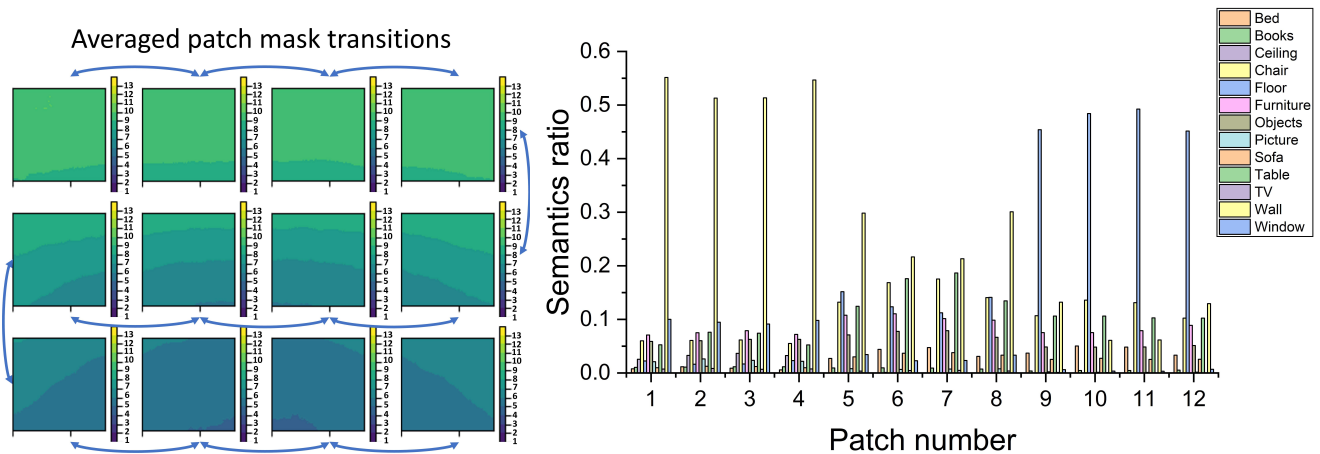


Figure 16. Left: Averaged patch mask transitions over SUN-RGBD test set; Right: Averaged patch semantics over SUN-RGBD test set



Figure 17. Demo of all types of corruptions

Algorithm 1 Patch shuffling

```

1: def shuffle(tensors, num_patch, ps):
2:   result ← []
3:   for it, X in enumerate(tensors) do
4:     patches ← nnF.unfold(X, ps, ps, 0)
5:     p ← patches.shape[-1]
6:     if it == 0 then
7:       indices ←
8:         sample(range(p), num_patch)
9:       orig ← tensor(range(p))
10:      perm ← tensor(range(p))
11:      for j in range(num_patch) do
12:        perm[indices[j]] =
13:          orig[indices[(j + 1)%num_patch]]
14:      end for
15:    end if
16:    patches ← concat(patch[:, perm]
17:                    for patch in patches)
18:    X ← nnF.fold(patches, X.shape[-2:],
19:                ps, ps, 0)
20:    result.append(X)
21:  end for
22:  Return result

```

Algorithm 2 Patch blackout

```

1: def shuffle(tensors, num_patch, ps):
2:   result ← []
3:   for it, X in enumerate(tensors) do
4:     patches ← nnF.unfold(X, ps, ps, 0)
5:     p ← patches.shape[-1]
6:     if it == 0 then
7:       indices ←
8:         sample(range(p), num_patch)
9:     end if
10:    for idx, X in enumerate(patches) do
11:      patches[idx][:, indices] ← 0
12:    end for
13:    X ← nnF.fold(patches, X.shape[-2:],
14:                ps, ps, 0)
15:    result.append(X)
16:  end for
17:  Return result

```

Figure 18. Patch shuffling and patch blackout algorithms

Algorithm 3 Patch blurring

```
1: def shuffle(tensors, num_patch, ps,
2:             kernel_size, sigma):
3:   result ← []
4:   blurrer = T.GaussianBlur(kernel_size, sigma)
5:   for it, X in enumerate(tensors) do
6:     patches ← nnF.unfold(X, ps, ps, 0)
7:     p ← patches.shape[-1]
8:     if it == 0 then
9:       indices ←
10:        sample(range(p), num_patch)
11:     end if
12:     for idx, X in enumerate(patches) do
13:       patches[idx][:, indices] ←
14:        blurrer(reshape(patches[idx][:, indices]))
15:     end for
16:     X ← nnF.fold(patches, X.shape[-2:],
17:                 ps, ps, 0)
18:     result.append(X)
19:   end for
20:   Return result
```

Algorithm 4 Create puzzles

```
1: def shuffle(tensors, num_perm, ps):
2:   result ← []
3:   for it, X in enumerate(tensors) do
4:     patches ← nnF.unfold(X, ps, ps, 0)
5:     p ← patches.shape[-1]
6:     if it == 0 then
7:       perms ← []
8:       for perm_id in range(num_perm) do
9:         perms.append(randperm(p))
10:      end for
11:    end if
12:    res ← X.clone()
13:    for perm in perms do
14:      new_patches ←
15:        concat(patch[:, perm]
16:              for patch in patches)
17:      new_X ←
18:        nnF.fold(patches, X.shape[-2:],
19:                ps, ps, 0)
20:      res ← concat(res, new_X)
21:    end for
22:    result.append(res)
23:  end for
24:  Return result
```

Figure 19. Patch blurring and creating puzzle algorithms

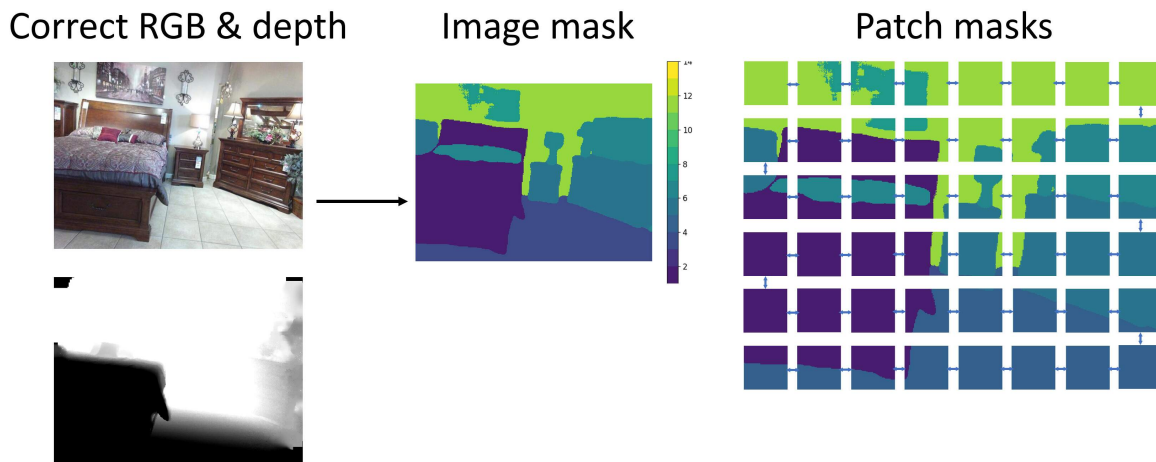


Figure 20. SUN-RGBD, patch size=80: sequence of correct image patch masks

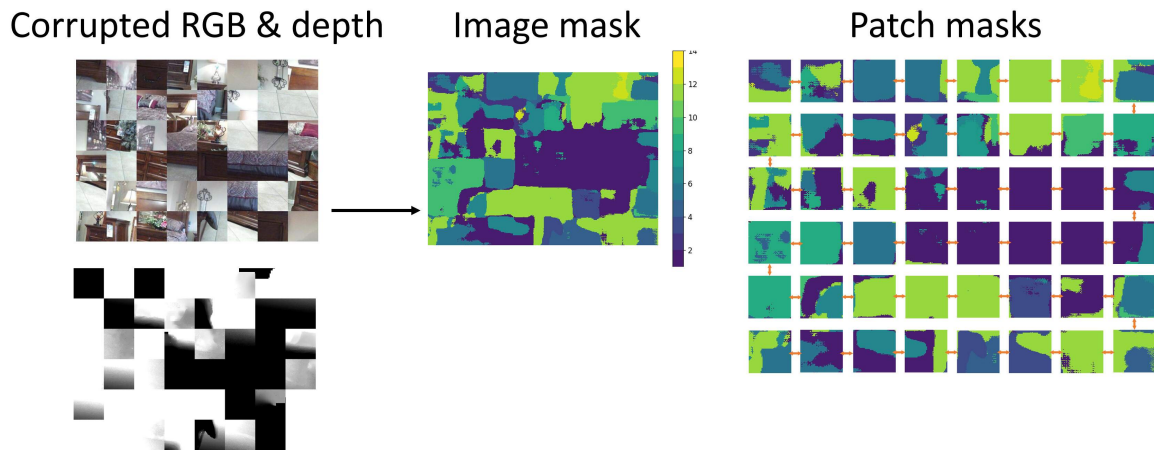


Figure 21. SUN-RGBD, patch size=80: sequences of corrupted image patch masks

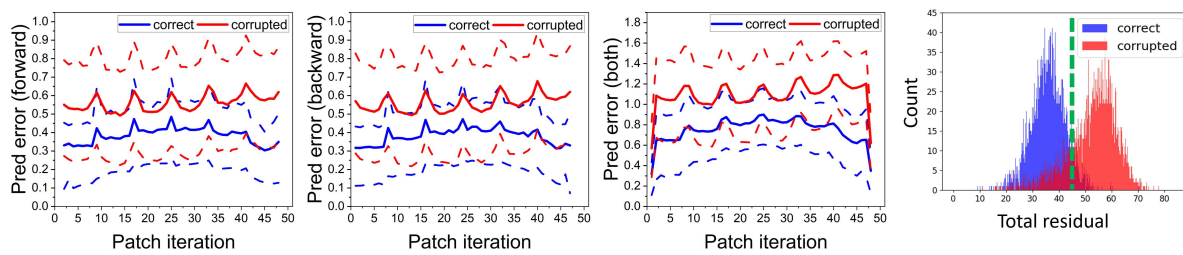


Figure 22. SUN-RGBD, patch size=80: forward, backward, and bi-directional LSTM prediction errors, histogram of total error (residual) over test samples (from left to right)